Biosensors and Bioelectronics 160 (2020) 112217

Contents lists available at ScienceDirect

Biosensors and Bioelectronics

journal homepage: http://www.elsevier.com/locate/bios

A novel high efficient electrochemiluminescence sensor based on reductive Cu(I) particles catalyzed Zn-doped MoS_2 QDs for HPV 16 DNA determination

Yixin Nie [a,b], Xin Zhang [a], Qian Zhang [a], Zihui Liang [a], Qiang Ma [a,*], Xingguang Su [a,**]

[a] Department of Analytical Chemistry, College of Chemistry, Jilin University, Changchun, 130012, China
[b] Electron Microscopy Center, Jilin University, Changchun, 130012, China

ARTICLE INFO

Keywords:
Zn-doped MoS_2 QDs
Visual electrochemiluminescence analysis
Reductive Cu(I) particles
DNA walker
HPV 16 DNA determination
ECL imaging

ABSTRACT

In this work, we explored a high efficient electrochemiluminescence (ECL) sensor based on the synergistic enhancement strategy of Zn-doped MoS_2 quantum dots (QDs) and reductive Cu(I) particles. On the one hand, Zn-doped MoS_2 QDs with sulfur vacancies were designed to improve the ECL activity of QDs. The regulated sulfur vacancies with zinc doping resulted in adsorption and coordination with transition metals of H_2O_2 as coreactant. On the other hand, reductive Cu(I) particles were prepared to further catalyze the coreactant in the ECL system. The tight combination of glutathione (GSH) and copper in reductive Cu(I) particles can perfectly stabilize Cu(I) with outstanding catalytic activity in neutral pH condition. Under reduction of the cathode, the reductive Cu(I) particles acted as the catalytic role continuously. As a result, more ·OH were generated from H_2O_2. The signal of Zn-doped MoS_2 QDs had 4.5-fold enhancement with the assistance of reductive Cu(I) particles. Furthermore, the DNA walker cycle was designed in presence of T7 exonuclease for HPV 16 DNA detection. The biosensor realized sensitive determination of HPV 16 DNA from 0.1 nmol L^{-1} to 200 nmol L^{-1} with the LOD of 0.03 nmol L^{-1}. Interestingly, the entire sensing system can be reproduced on a simple family-friendly device powered by batteries. The ECL signal captured by a smartphone can be processed into high-resolution imaging by self-developed software, which provides great possibility of point-of-care HPV 16 DNA determination in the future.

1. Introduction

Cervical cancer is the most common gynecological malignancy. Carcinoma in situ and invasive cancer has a high incidence in women aged 30–35 years and 45–55 years, respectively. In recent years, the disease has a tendency to occur in younger people. Every year around 500,000 people worldwide suffer from cervical cancer and the mortality rate is extremely high (Parkin et al., 2001). As we all know, the main cause of cervical cancer is the persistent infection of human papilloma virus (HPV) high-risk types 16 and 18 (Walboomers et al., 1999; Bosch et al., 2002; Davies et al., 2001; Van Den Brule et al., 2002). Since about 80% of patients come from countries with poor public health resources, and current HPV DNA testing methods rely on expensive equipment with long waiting time for test results, a family-friendly fast determination method is of necessity.

Electrochemiluminescence (ECL) is an ideal method in sensing analysis system due to its low background signal and excellent time control ability without light source (Tan et al., 2017; Liu et al., 2015; Yang et al., 2017a,b; Xing et al., 2018; Yang et al., 2017a, 2017b), which has been widely used in clinical tests (Zhou et al., 2018; M.M. Chen et al., 2018a; Wu et al., 2014; Chen et al., 2018a, 2018b; X. Chen et al., 2018b). In recent years, some novel QDs (e.g. graphene QDs and MoS_2 QDs) with low toxicity and high biocompatibility (Presolski and Pumera, 2016) have gradually become popular in hydrogen evolution catalysis, electrochemical sensors, photodynamic therapy and bioimaging (Dong et al., 2016; Ren et al., 2015; Dai et al., 2015a, b; Sweet et al., 2017; Cao et al., 2017). However, the ECL signal of those QDs in common coreactant H_2O_2 is relatively weak. Firstly, the ECL yields of these traditional QDs are quite low. Although many methods about improving quantum yields of QDs have been developed, the poor electrochemical reaction activity of QDs with coreactant still limits enhancement of ECL. Secondly, H_2O_2 as common coreactant is unstable

* Corresponding author.
** Corresponding author.
E-mail addresses: qma@jlu.edu.cn (Q. Ma), suxg@jlu.edu.cn (X. Su).

https://doi.org/10.1016/j.bios.2020.112217
Received 15 February 2020; Received in revised form 23 March 2020; Accepted 14 April 2020
Available online 19 April 2020

and easily decomposes. Although more ·OH can be generated by Fenton reaction (Ma et al., 2019), how to promote the production of ·OH with high efficiency in ECL is still an essential topic. For example, many metal catalysts (Fe, Al, Ce, Co, Cu, Ru, etc) can generate ·OH based on the Fenton reaction. However, Fe and Al catalysts have strict requirements on pH condition (Ma et al., 2019; Bokare and Choi, 2014). Ce catalyst with high toxicity is harmful to the environment (Asati et al., 2010). Co catalyst also has huge stoichiometric requirement of H_2O_2. And Ru catalyst has expensive cost (Bokare and Choi, 2014). Although inexpensive and low-toxic Cu^+ catalyst can easily generate ·OH in neutral pH condition, it is easily oxidized by dissolved oxygen in water (Bokare and Choi, 2014). Therefore, it is an urgent need to develop high efficient QD-based ECL sensor with reliable catalytic reaction.

In recent years, DNA nanomachines such as DNA tweezers (Elbaz et al., 2009), DNA scissors (Peng et al., 2019), DNA gears (Zhang et al., 2017), etc., especially which imitate the motion of biological protein motors, have been widely used as ideal amplification strategies for ECL signals (Liu et al., 2018). The high sensitivity of these strategies also provides the possibility for point-of-care determination. The new generation of smartphones with multiple sensing modules, especially advanced CMOS image sensors, have prompted the development of variable point-of-care devices (Choi, 2016; Gao and Wu, 2016; Adiguzel and Kulah, 2012; Dutta, 2019).

In this work, we designed the ECL sensing system based on Zn-doped MoS_2 QDs assisted with reductive Cu(I) particles (as shown in Scheme 1). On the one hand, zinc doping was employed to regulate the conductivity and ECL yield of QDs. Meanwhile, zinc doping was confirmed to generate sulfur vacancies through a series of characterizations, which were closely related to the coreactant H_2O_2 in ECL system (Zhang et al., 2014, 2019). As a result, H_2O_2 can attach to the sulfur vacancies and coordinate with transition metal ions. It ultimately led to the amplification of ECL signal and the improvement of ECL efficiency of QDs. On the other hand, the self-assembled reductive Cu(I) particles were first prepared to catalyze the coreactant. The reductive Cu(I) particles can promote the generation of ·OH from coreactant H_2O_2. More importantly, the combination of GSH and copper overcame the shortcoming of traditional copper catalysts which were easily oxidized and lost effectiveness. Meanwhile, reductive Cu(I) particles have shown the superiority in ECL system, which can be reduced to the original valence state by the cathode to continuously provide further assistance for ECL elevation. Furthermore, an enzyme-assisted DNA walker cycle was explored to efficiently amplify ECL signal on the electrode surface for point-of-care target determination. The reductive Cu(I) particles with arm-DNA and cDNA were immobilized on the electrode surface. After pDNA and QD-DNA were introduced and hybridized, the biosensing system had strong ECL signal in N_2-saturated H_2O_2. When target HPV 16 DNA was captured by cDNA, the arm-DNA was bound to the QD-DNA. Under the incubation of T7 exonuclease, the bonding between QD-DNA and arm-DNA was cut off, releasing the arm-DNA as the DNA walker to bind to the next QD-DNA. During the cycling action of the DNA walker, Zn-doped MoS_2 QDs were continuously released from the electrode surface. Therefore, the quenching effect of ECL signal was amplified. Moreover, in the sensing process, a series of ECL images processed through software intuitively exhibited distinguishable signals, which opens up huge possibilities for HPV 16 DNA point-of-care determination.

2. Experimental section

2.1. Synthesis of Zn-doped MoS_2 QDs and QD-DNA

0.0234 g of ammonium molybdate tetrahydrate, 0.1268 g of reduced glutathione, and 0.0592 g of zinc nitrate hexahydrate were dissolved in 6.5 mL of ultrapure water. It was heated at 180 °C for 40 min with the assistance of microwave. The green mixture was centrifuged (10,000 rpm, 10 min). 40 μL of activated Zn-doped MoS_2 QDs solution was mixed with 30 μL of 100 μM DNA solution (total volume 1 mL). After stirring for 3 h, it was stored in the refrigerator for later use.

2.2. Preparation of reductive Cu(I) particles

1 mmol of sodium hydroxide and 1 mmol of reduced glutathione were dissolved in 5 mL of ultrapure water. The mixture was dropped into 5 mL of copper sulfate solution (0.5 mmol). The solution quickly changed from light blue to suspension containing white particles. After 5 min of stirring at room temperature, the mixture was centrifuged (6000 rpm, 3 min) and washed with water. The obtained white solid was stored in absolute ethanol.

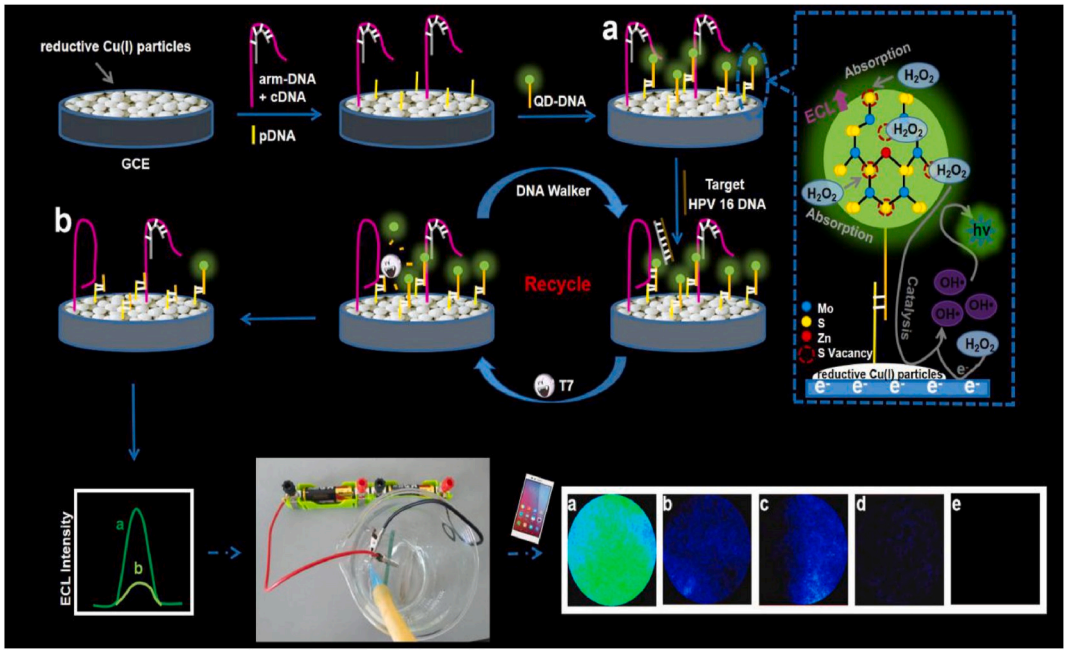

Scheme 1. Schematic illustration of reductive Cu(I) particles catalyzed Zn-doped MoS_2 QD-based ECL biosensor.

2.3. Synthesis of mixture of arm-DNA and cDNA and establishment of biosensor

0.5 mL of 900 nM arm-DNA solution was mixed with 0.5 mL of 900 nM cDNA solution. The mixture was heated at 95 °C for 5 min. It was then slowly cooled as room temperature. The mixture was placed in the refrigerator for use. 10 μg mL^{-1} reductive Cu(I) particles solution was dropped on the glassy carbon electrode (GCE). After drying, 2 μL of the mixture solution of arm-DNA and cDNA and 3 μL of 3 μM pDNA were dropped on the surface. After the mercapto group was successfully bound to the complex, 3 μL of QD-DNA solution was added and incubated for 2 h. After HPV 16 DNA with different concentrations was added for 2 h, the electrode surface was washed with PBS. 50 U mL^{-1} T7 exonuclease (with 1 × NE buffer 4) was dropped and incubated for 2 h. The electrode was then rinsed with 1 × TE buffer and dried for ECL measurement. The measurements were achieved in N_2-saturated 5 mM PBS (pH 7.4) containing 10 mM H_2O_2.

2.4. Visual inspection

The entire device consisted of two dry batteries, 6 cm × 5 cm FTO glass (working electrode), platinum wire (counter electrode), and a smartphone. The response environment of the biosensing system remained unchanged. The entire imaging process took place with assistant of a dark box. Finally, a series of photos taken by the CMOS sensor chip (1920 × 1080 pixels) embedded in the smartphone camera were processed into high-resolution images with self-developed software.

3. Results and discussion

3.1. Characterization of Zn-doped MoS_2 QDs

The reaction time, temperature, and raw material ratio of the microwave-assisted synthesis of Zn-doped MoS_2 QDs were optimized (as shown in Fig. S1). The TEM images from Fig. 1 and Fig. S2 showed that both Zn-doped MoS_2 QDs and the original MoS_2 QDs had uniform size and perfect dispersibility. The particle size of Zn-doped MoS_2 QDs was ca. 3.6 nm, which was slightly smaller than the original MoS_2 QDs (ca. 4 nm). Fig. S1 exhibited that the color of Zn-doped MoS_2 QDs solution gradually changed from yellow to green with the increase of the amount of zinc. XPS spectra of Zn-doped MoS_2 QDs and MoS_2 QDs were compared in Fig. 1 and Fig. S2, which confirmed the successful doping of zinc element. Mo 3d peaks of MoS_2 QDs and Zn-doped MoS_2 QDs located at about 228.1 eV and 230.7 eV, indicating that Mo^{6+} was successfully reduced to form MoS_2 QDs. The extra peak at 229.4 eV after doping represented Mo^{n+} ($n < 4$), confirming the further reduction of Mo. The Mo^{6+} peaks at 235.5 eV and 232.5 eV were originated from oxidation of Mo during long-term storage (Huang et al., 2018). S 2p peaks of MoS_2 QDs and Zn-doped MoS_2 QDs located at about 163.5 eV and 165.0 eV. Negative shifts in binding energies of the S 2p states after doping respectively indicated increase of electronic density of QDs (Wu et al., 2018; Yin et al., 2019). The molar ratio of S and Mo decreased after doping, which indicated the departure of S and the formation of S vacancies (Wu et al., 2018). From the XRD patterns (Fig. S3), the Bragg peak of Zn-doped MoS_2 QDs moved to the larger 2θ, according to the Bragg formula ($2d\sin\theta = n\lambda$), which confirmed that zinc doping brought about the unit cell shrinkage of QDs (Pan et al., 2019).

The characterization of the UV–vis pattern (Fig. S4A) exhibited the apparent blue-shift of the absorption edge of Zn-doped MoS_2 QDs. Since the doped Zn^{2+} has fewer valence electrons than the Mo^{4+} in the QDs, the doping was inferred as p-type doping. Therefore, the blue shift of the absorption edge was attributed to the quantum confinement effect compared to the Burstein-Moss effect (Majeed Khan et al., 2017; He et al., 2012). The comparison of the FT-IR spectrum (Fig. S4B) confirmed that the functional groups of two kinds of QDs had no significant change. The two peaks above 3000 cm^{-1} were both attributed to N–H and O–H. And both of QDs had the C═O peak at 1600-1870 cm^{-1}, which was consistent with the negative zeta potential of two kinds of QDs. Both the maximum emission peak position and the wavelength-dependent phenomenon in the fluorescence properties of Zn-doped MoS_2 QDs (as exhibited in Fig. S5) were consistent with the original MoS_2 QDs.

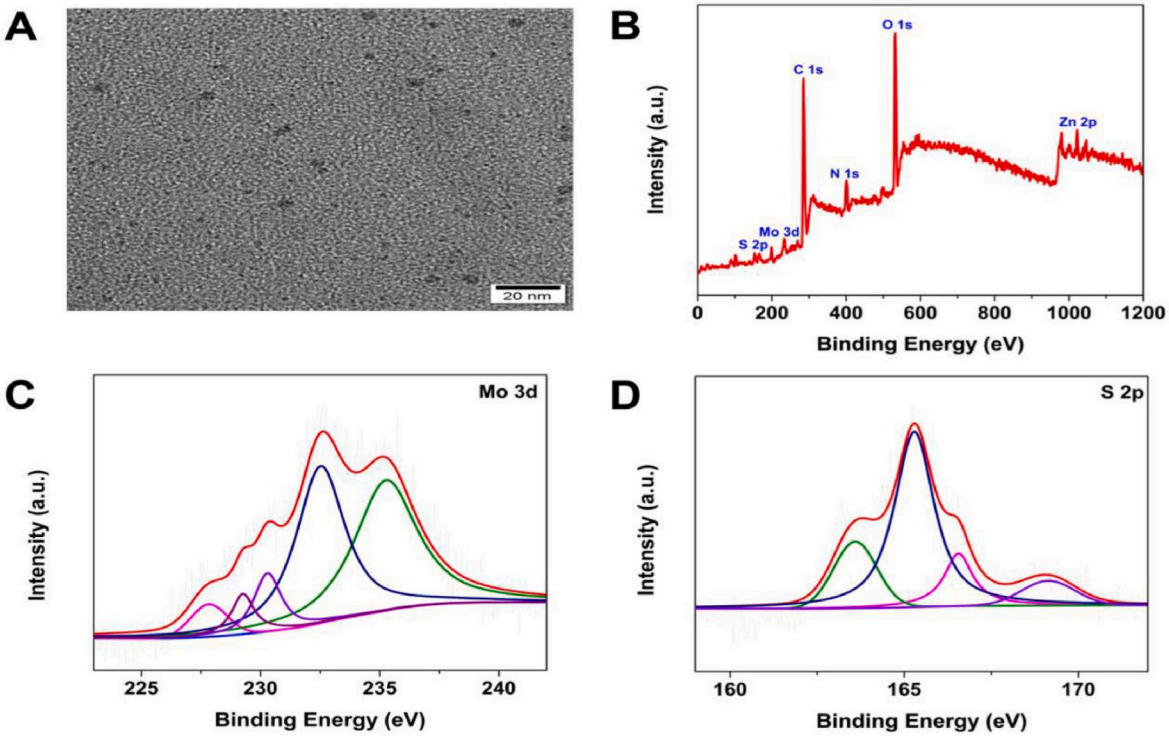

Fig. 1. (A) TEM and (B, C, and D) XPS images of Zn-doped MoS_2 QDs.

Zn-doped MoS_2 QDs emitted ca. 7-time fluorescence intensity over the original MoS_2 QDs at the same excitation wavelength (as showed in Fig. S4C). The intensity contrast was particularly obvious under night-time ultraviolet lamp (as exhibited in Fig. S4D). After Zn atom doping, surface trap states of QDs were modified due to recombination of defects and excitation states, which highly boosted the fluorescence intensity (Yang et al., 2002). Fig. 2 showed the comparison of ECL performance of Zn-doped MoS_2 QDs and MoS_2 QDs. The ECL peak of Zn-doped MoS_2 QDs was at 555 nm. The maximum ECL intensity of Zn-doped MoS_2 QDs with H_2O_2 was ca. 3-time over that of the original MoS_2 QDs. It indicated the adsorption of H_2O_2 molecules (coordination with transition metal ions Zn^{2+}, Mo^{4+}) due to sulfur vacancies. And the ·OH was fixed on the QDs, leading to the stable enhancement of ECL emission (Zhang et al., 2014). The excitation potential of Zn-doped MoS_2 QDs (−2.3 V) was smaller than that of the MoS_2 QDs (−2.4 V), which was consistent with the theory that the carrier density increased due to sulfur vacancies.

3.2. Characterization of reductive Cu(I) particles

The TEM image (Fig. 3A) characterized the reductive Cu(I) particles as spherical particles with the diameter of about 600 nm. There was some aggregation of reductive Cu(I) particles due to the interaction of groups (Hua et al., 2019). The similar aggregation of metal catalytic materials has been reported in previous paper (Ma et al., 2019). The absorption peak of reductive Cu(I) particles in the UV–vis spectrum (Fig. 3B) changed significantly compared with the copper salt solution and the reduced glutathione solution, which confirmed the successful formation of reductive Cu(I) particles. Compared to the FT-IR spectra of $CuSO_4$ and GSH (Fig. S6), the peaks of N–H and O–H above 3000 cm^{-1} and the peak of C═O at 1600-1870 cm^{-1} in the FT-IR spectra (Fig. 3C) of reductive Cu(I) particles were related to GSH. The peak (2550 cm^{-1}) symbolizing S–H disappeared in the FT-IR spectra of reductive Cu(I) particles, indicating that S was bound to Cu, which further confirmed the successful formation of reductive Cu(I) particles. The XPS peaks of Cu 2p (Fig. 3D) at 931.8 eV and 951.7 eV represented Cu^+ $2p_{3/2}$ and Cu^+ $2p_{1/2}$ respectively, indicating the formation of Cu^+. In reductive Cu(I) particles, the stability and the catalytic activity of Cu(I) was largely improved. Thiol group of GSH can stably combine with copper element, which improved the stability of the material. GSH also protected the catalytic activity of Cu(I). The reductive Cu(I) particles can be stored in ethanol for more than one month with excellent catalytic activity. In order to test the catalytic effect of reductive Cu(I) particles, reductive Cu (I) particles and H_2O_2 were added into methylene blue (MB) solution. The ultraviolet absorption intensity of the mixture solution decreased with time until the color completely disappeared (as exhibited in Fig. 4A). In contrast, MB solution containing only reductive Cu(I) particles and H_2O_2 separately cannot be degraded after a period of time. The above results revealed that the interaction of reductive Cu(I) particles and H_2O_2 can produce ·OH (strong oxidative degradation substance), which can be accurately explained by Fenton reaction (Ma et al., 2019).

3.3. Catalysis-assisted ECL mechanism

The cyclic voltammogram (Fig. 4B) and potential-ECL diagrams (Fig. 4C) confirmed the catalytic effect of reductive Cu(I) particles with the unchanged potential position. The catalytic action (as revealed in Fig. 4D) was reflected in the increase of ECL of Zn-doped MoS_2 QDs (ca. 50%), which indicated that more ·OH generated by catalysis of reductive Cu(I) particles in N_2-saturated H_2O_2 promoted the QDs to emit stronger ECL after being excited. In this ECL system, the cathode can continuously supply electrons to reductive Cu(I) particles (Jia et al., 2019; Ma et al., 2019), which led to Cu(II) be reduced to the original valence state and generate ·OH.

The mechanism reactions were as follows:

$$Cu(I) + H_2O_2 \rightarrow Cu(II) + \cdot OH + OH^- \quad (1)$$

$$Cu(II) + e^- \rightarrow Cu(I) \quad (2)$$

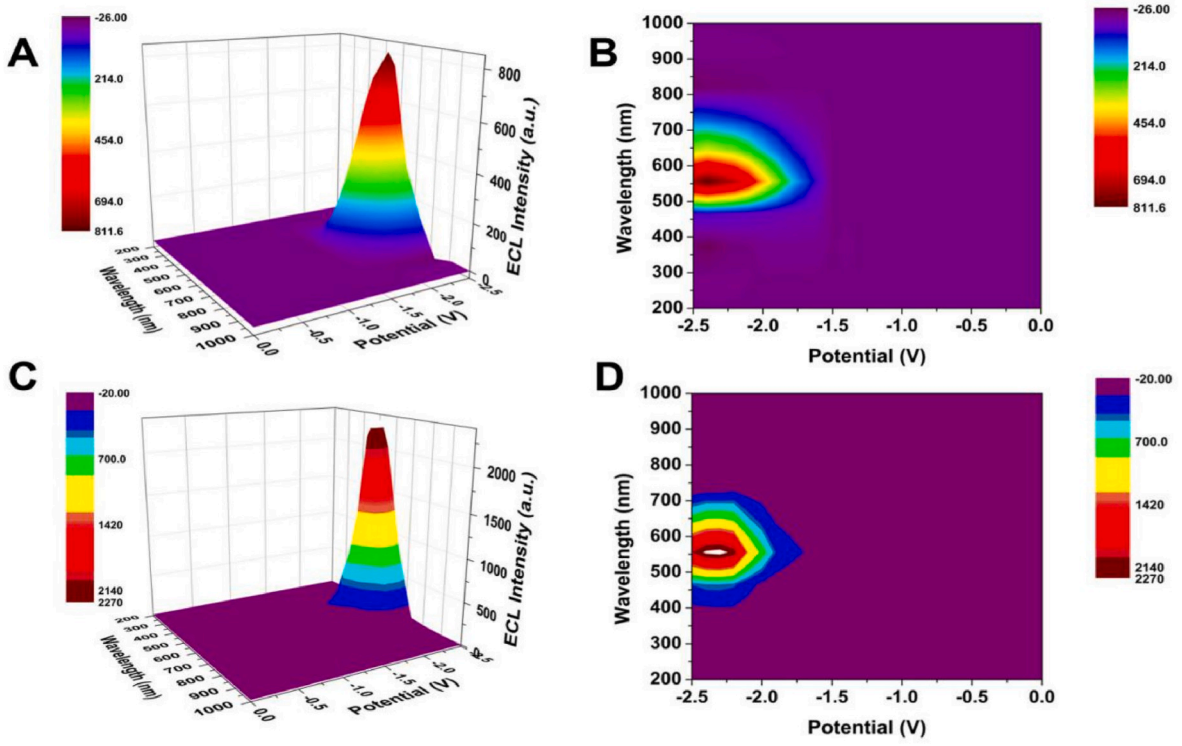

Fig. 2. The three-dimensional graphs of ECL intensity at different potentials and wavelengths of MoS_2 QDs (A, B) and Zn-doped MoS_2 QDs (C, D) in N_2-saturated 5 mM PBS (pH 7.4) containing 10 mM H_2O_2.

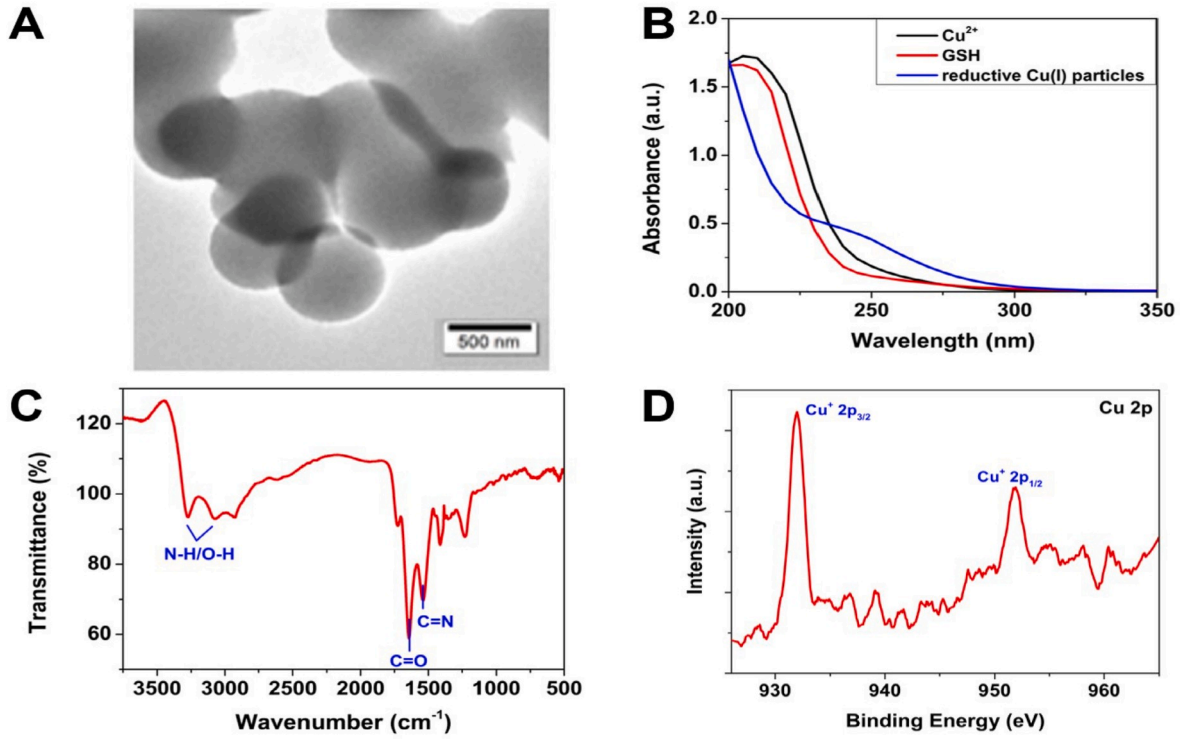

Fig. 3. (A) TEM, (B) UV–vis absorption, (C) FT-IR and (D) XPS spectra of reductive Cu(I) particles.

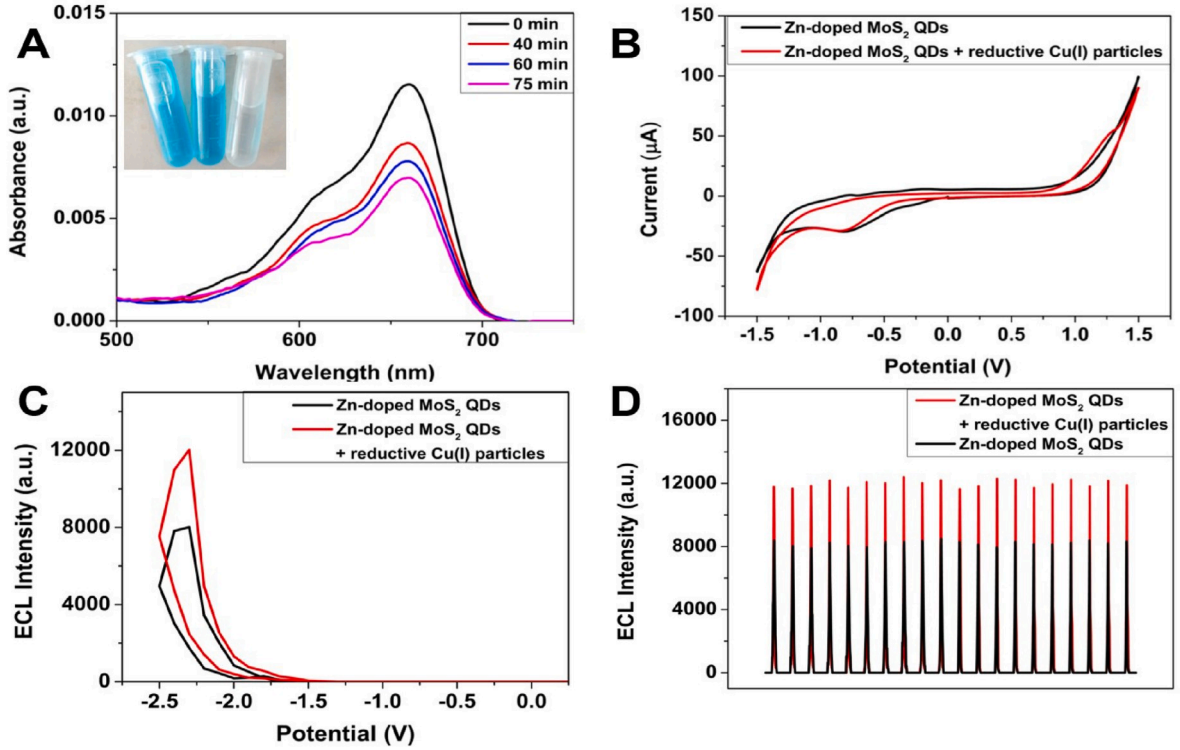

Fig. 4. (A) UV–vis absorption spectra of MB under different reaction time after adding reductive Cu(I) particles and H_2O_2 (insert: from left to right: adding reductive Cu(I) particles, H_2O_2, and reductive Cu(I) particles with H_2O_2). (B) Cyclic voltammetry curve, (C) potential-ECL intensity curve and (D) ECL stability of Zn-doped MoS_2 QDs and Zn-doped MoS_2 QDs/reductive Cu(I) particles in N_2-saturated 5 mM PBS (pH 7.4) containing 10 mM H_2O_2.

$$H_2O_2 + e^- \xrightarrow{\text{reductive Cu(I) particles}} \cdot OH + OH^- \quad (3)$$

$$\cdot OH + QD + e^- \rightarrow QD^* + OH^- \quad (4)$$

$$QD^* \rightarrow QD + hv \quad (5)$$

3.4. DNA walker cycle amplification for HPV determination

A series of reaction conditions of the biosensing system were optimized. From the ECL curve (Fig. S7A), it can be seen that with the increase of the concentration of the added Zn-doped MoS_2 QDs, the ECL intensity gradually increased and reached the maximum. With the addition of excessive QDs, the ECL of QDs can be quenched due to the self-aggregation. The concentration of H_2O_2 can also effect the ECL intensity of QDs as revealed in Fig. S7B. The ECL intensity of QDs reached the maximum when the concentration of H_2O_2 reached 10 mM. More H_2O_2 caused excessive free radicals to eliminate each other (Dai et al., 2015a). In addition, the action time of T7 exonuclease was optimized. As exhibited in Fig. S7C, when the action time was 2 h, the reaction almost completed. Therefore 2 h was chosen as the optimal action time. The feasibility of the biosensing system was tested as shown in Fig. 5A. After hybridization of mixture of arm-DNA and cDNA, pDNA and QD-DNA, the ECL intensity of Zn-doped MoS_2 QDs in H_2O_2 catalyzed by reductive Cu(I) particles greatly increased. In the detection of target HPV 16 DNA, the ECL intensity decreased sharply due to the release of QDs from the electrode surface via the cutting action of T7 exonuclease. Similarly, the EIS image (Fig. 5B) also revealed the realization of the biosensing system. The impedance of the bare electrode was low, which increased with the addition of reductive Cu(I) particles to 1300 Ω. When pDNA and the mixture of arm-DNA and cDNA were introduced, the impedance further increased to 2600 Ω. The addition of QD-DNA maximized the impedance to 5300 Ω. After T7 exonuclease cuted QD-DNA out, the impedance was reduced to about the same as that without QDs. In the corresponding cyclic voltammetry graph (Fig. S8), after both reductive Cu(I) particles and QDs were modified on the electrode surface, the potential difference increased and the current decreased, which also confirmed successful construction of the sensor. In the target DNA sensing process, the potential difference and current gradually recovered, indicating that QD-DNA was successfully cut off. In addition, the prepared sensor showed long-term stability (as revealed in Fig. S9). ECL signal of the sensor remained unchanged for two days after it was successfully produced. After three days, due to reductive Cu(I) particles being oxidized in the air quenched the ECL of QDs, the ECL signal decreased slightly.

With the well-established biosensing system, the quantitative analysis of HPV 16 DNA with different concentrations was carried out. The linear quantitative determination (Fig. 5C) of HPV 16 DNA with concentrations ranging from 0.1 nmol L^{-1} to 200 nmol L^{-1} was achieved with the LOD of 0.03 nmol L^{-1} (Fig. 5D). In addition, the results of selectivity experiments (Fig. S10) exhibited that HPV 18 DNA, HPV 31 DNA, and HPV 33 DNA at 200 nmol L^{-1} cannot be responded in the biosensing system as the same concentration of HPV 16 DNA. In Table S1, the detection results of the human serum (from Third Hospital of Jilin University) also proved the feasibility of the biosensing system (recovery range 99%–106%, RSD ≤ 4.11%). Moreover, compared with other analytical methods, the proposed ECL biosensor had wider determination range and lower LOD (as shown in Table S2).

In response to the requirement of point-of-care testing, a miniaturized ECL device composed of two dry batteries in series was designed for HPV 16 DNA testing. The specific connection method was shown in Fig. S11. Under unchanged testing conditions, the entire device was put in a dark box with a smartphone for imaging and self-software for data analysis. The results revealed that when concentration of HPV 16 DNA was from 0.1, 10, 50, 100–200 nmol L^{-1}, the images taken by the smartphone (Fig. S12) were not clear. After processed by the self-developed software, the high-resolution images (Fig. 5E) had obvious

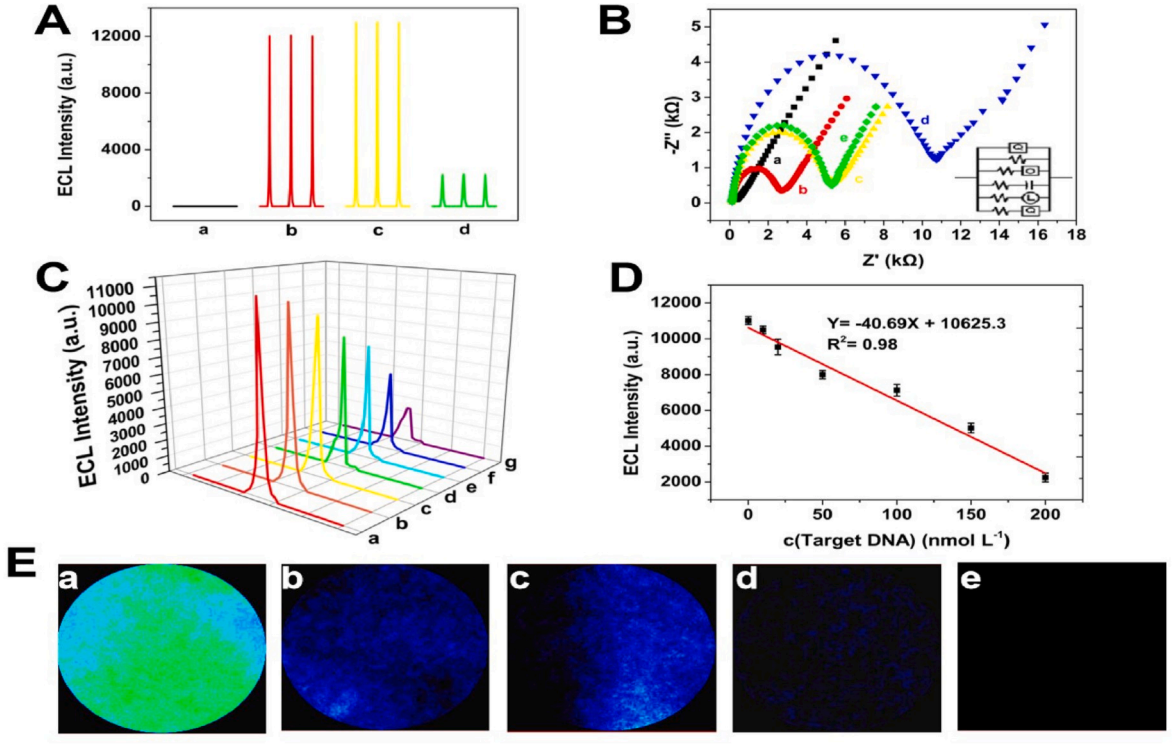

Fig. 5. (A) The ECL performance and (B) EIS curve and the equivalent circuit in the sensing system construction. (C) ECL response of the biosensor with (a) 0.1 nM, (b) 1 nM, (c) 10 nM, (d) 20 nM, (e) 50 nM, (f) 100 nM and (g) 200 nM HPV 16 DNA. (D) ECL linear relationship of HPV 16 DNA detection. (E) Visualized ECL images processed by the self-developed software with (a) 0.1 nM, (b) 10 nM, (c) 50 nM, (d) 100 nM and (e) 200 nM HPV 16 DNA.

change, which showed the realization of point-of-care determination of HPV 16 DNA. In the near future, such a miniaturized device with a smartphone for home-based testing will greatly assist the full popularization of point-of-care testing.

4. Conclusions

In summary, the high efficient ECL system with synergy of zinc doping and catalyst reductive Cu(I) particles successfully improved the signal of QDs. Zn-doped MoS_2 QDs had more excellent ECL properties due to sulfur vacancies with adsorption of coreactant H_2O_2. Meanwhile, the reductive Cu(I) particles catalyzed the coreactant H_2O_2 for stronger ECL of the system. In the practical biosensing system for HPV 16 DNA determination, the enzyme-assisted DNA walker strategy was designed for the determination of HPV 16 DNA from 0.1 nmol L^{-1} to 200 nmol L^{-1} with the LOD of 0.03 nmol L^{-1}. More importantly, the entire testing process can be reproduced in a home-based miniaturized device and read by a smartphone software. This provides meaningful ideas for point-of-care testing of HPV 16 DNA in the future. Although the entire process of detecting by professional instruments was realized in a miniaturized device, tediousness of sample pretreatment is still a problem to be solved in the future. We will dedicate to work towards the successful spread of fully point-of-care testing.

Declaration of competing interest

The authors declare that they have no known competing financial interests or personal relationships that could have appeared to influence the work reported in this paper.

CRediT authorship contribution statement

Yixin Nie: Conceptualization, Data curation, Formal analysis, Funding acquisition, Investigation, Methodology, Project administration, Resources, Software, Supervision, Validation, Visualization, Writing - original draft, Writing - review & editing. **Xin Zhang:** Project administration, Resources. **Qian Zhang:** Software, Supervision. **Zihui Liang:** Visualization. **Qiang Ma:** Writing - original draft. **Xingguang Su:** Writing - original draft.

Acknowledgments

The work was supported by the National Natural Science Foundation of China (No. 21775052 and No. 21575048), the Science and Technology Development project of Jilin province, China (No. 20180414013 GH).

Appendix A. Supplementary data

Supplementary data to this article can be found online at https://doi.org/10.1016/j.bios.2020.112217.

References

Adiguzel, Y., Kulah, H., 2012. Sensors 12, 10042–10066.
Asati, A., Santra, S., Kaittanis, C., Perez, J.M., 2010. ACS Nano 4, 5321–5331.
Bokare, A.D., Choi, W.Y., 2014. J. Hazard Mater. 275, 121–135.
Bosch, F.X., Lorincz, A., Munoz, N., Meijer, C.J., Shah, K.V.J., 2002. Clin. Pathol. 55, 244–265.
Cao, H., Wang, H., Huang, Y., Sun, Y., Shi, S., Tang, M., 2017. Microchim. Acta. 184, 91–100.
Chen, M.M., Wang, Y., Cheng, S.B., Wen, W., Zhang, X., Wang, S., Huang, W.H., 2018a. Anal. Chem. 90, 5075–5081.
Chen, X., Gui, W., Ma, Q., 2018b. Anal. Chim. Acta 1009, 73–80.
Choi, S., 2016. Biotechnol. Adv. 34, 321–330.
Dai, P., Yu, T., Shi, H., Xu, J., Chen, H., 2015a. Anal. Chem. 87 (24), 12372–12379.
Dai, W., Dong, H., Fugetsu, B., Cao, Y., Lu, H., Ma, X., Zhang, X., 2015b. Small 11, 4158–4164.
Davies, P., Kornegay, J., Iftner, T., 2001. Best Pract. Res. Clin. Obstet. Gynaecol. 15, 677–700.
Dong, H., Tang, S., Hao, Y., Yu, H., Dai, W., Zhao, G., Cao, Y., Lu, H., Zhang, X., Ju, H., 2016. ACS Appl. Mater. Interfaces 8, 3107–3114.
Dutta, S., 2019. Trends Anal. Chem. 110, 393–400.
Elbaz, J., Moshe, M., Willner, I., 2009. Angew. Chem. 121, 3892–3895.
Gao, X., Wu, N., 2016. Electrochem. Soc. Interface 25, 79–81.
He, X., Demchenko, I.N., Stolte, W.C., Buuren, A., Liang, H., 2012. J. Phys. Chem. C 116, 22001–22008.
Hua, Y., Liu, M., Li, S., Liu, F.J., Cai, Y.Y., Liu, H., Wan, Y.Q., Lv, X.X., Wang, H., 2019. Biosens. Bioelectron. 124, 89–95.
Huang, L.B., Zhao, L., Zhang, Y., Chen, Y.Y., Zhang, Q.H., Luo, H., Zhang, X., Tang, T., Gu, L., Hu, J.S., 2018. Adv. Energy Mater. 8, 1800734.
Jia, Y., Yang, L., Xue, J.W., Ren, X., Zhang, N., Fan, D.W., Wei, Q., Ma, H.M., 2019. Biosens. Bioelectron. 144, 111676.
Liu, Z., Qi, W., Xu, G., 2015. Chem. Soc. Rev. 44, 3117–3142.
Liu, J., Tang, Z., Zhang, J., Chai, Y., Zhuo, Y., Yuan, R., 2018. Anal. Chem. 90 (8), 5298–5305.
Ma, B., Wang, S., Liu, F., Zhang, S., Duan, J., Li, Z., Kong, Y., Sang, Y., Liu, H., Bu, W., Li, L., 2019. J. Am. Chem. Soc. 141, 849–857.
Majeed Khan, M.A., Khan, W., Ahamed, M., Alhazaa, A.N., 2017. Sci. Rep. 7, 12560.
Pan, Q., Yang, K., Wang, G., Li, D., Sun, J., Yang, B., Zou, Z., Hu, W., Wen, K., Yang, H., 2019. Chem. Eng. J. 372, 399–407.
Parkin, D.M., Bray, F., Ferlay, J., Pisani, P., 2001. Int. J. Canc. 94, 153–156.
Peng, L., Yuan, Y., Fu, X., Fu, A., Zhang, P., Chai, Y., Gan, X., Yuan, R., 2019. Anal. Chem. 91 (5), 3239–3245.
Presolski, S., Pumera, M., 2016. Mater. Today 192016, 140–145.
Ren, X., Pang, L., Zhang, Y., Ren, X., Fan, H., Liu, S., 2015. J. Mater. Chem. A. 3, 10693–10697.
Sweet, C., Pramanik, A., Jones, S., Ray, P.C., 2017. ACS Omega 2, 1826–1835.
Tan, X., Zhang, B., Zou, G., 2017. J. Am. Chem. Soc. 139, 8772–8776.
Van Den Brule, A.J.C., Pol, R., Fransen-Daalmeijer, N., Schouls, L.M., Meijer, C.J.L.M., Snijders, P.J.J., 2002. Clin. Microbiol. 40, 779–787.
Walboomers, J.M.M., Jacobs, M.V., Manos, M.M., Bosch, F.X., Kummer, J.A., Shah, K.V., Snijders, P.J.F., Peto, J., Meijer, C.J.L.M., Munoz, N., 1999. J. Pathol. 189, 12–19.
Wu, M.S., He, L.J., Xu, J.J., Chen, H.Y., 2014. Anal. Chem. 86, 4559–4565.
Wu, Y., Li, F., Chen, W., Xiang, Q., Ma, Y., Zhu, H., Tao, P., Song, C., Shang, W., Deng, T., Wu, J., 2018. Adv. Mater. 20, 1803151.
Xing, B., Zhu, W.J., Zheng, X.P., Zhu, Y.Y., Wei, Q., Wu, D., 2018. Sens. Actuators, B 265, 403–411.
Yang, L., Li, Y.Y., Zhang, Y., Fan, D.W., Pang, X.H., Wei, Q., Du, B., 2017a. ACS Appl. Mater. Interfaces 9, 35260–35267.
Yang, L., Zhu, W.J., Ren, X., Khan, M.S., Zhang, Y., Du, B., Wei, Q., 2017b. Biosens. Bioelectron. 91, 842–848.
Yang, P., Lu, M.K., Song, C.F., Xu, D., Yuan, D.R., Cheng, X.F., Zhou, G.J., 2002. Opt. Mater. 20, 141.
Yin, Y., Han, J., Zhang, Y., Zhang, X., Xu, P., Yuan, Q., Samad, L., Wang, X., Wu, W.Z., Niu, C.Y., Wei, C., Jia, Y., Li, C., Xu, Q., 2019. Angew. Chem. Int. Ed. 58 (7), 2029–2033.
Zhang, P., Lin, Z., Zhuo, Y., Yuan, R., Chai, Y., 2017. Anal. Chem. 89, 1338–1345.
Zhang, Q., Liu, Y., Nie, Y., Liu, Y., Ma, Q., 2019. Anal. Chem. 91, 13780–13786.
Zhang, Y., Zhou, H., Wu, P., Zhang, H., Xu, J., Chen, H., 2014. Anal. Chem. 86, 8657–8664.
Zhou, Y., Yu, Y., Chai, Y., Yuan, R., 2018. Talanta 181, 32–37.